



Cite as

Nano-Micro Lett.

(2020) 12:163

Received: 23 May 2020

Accepted: 9 July 2020

© The Author(s) 2020

# Secondary-Atom-Doping Enables Robust Fe–N–C Single-Atom Catalysts with Enhanced Oxygen Reduction Reaction

Xin Luo<sup>1</sup>, Xiaoqian Wei<sup>1</sup>, Hengjia Wang<sup>1</sup>, Wenling Gu<sup>1</sup>, Takuma Kaneko<sup>2</sup>, Yusuke Yoshida<sup>2</sup>, Xiao Zhao<sup>2</sup> ✉, Chengzhou Zhu<sup>1</sup> ✉

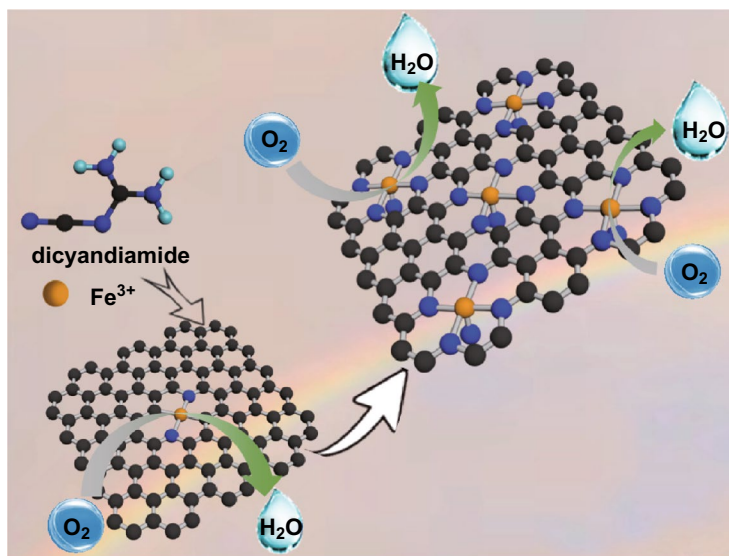
✉ Xiao Zhao, xiaozhao@uec.ac.jp; Chengzhou Zhu, czzhu@mail.ccnu.edu.cn

<sup>1</sup> Key Laboratory of Pesticide and Chemical Biology of Ministry of Education, International Joint Research Center for Intelligent Biosensing Technology and Health, College of Chemistry, Central China Normal University, Wuhan 430079, People's Republic of China<sup>2</sup> Innovation Research Center for Fuel Cells, The University of Electro-Communications, Chofugaoka, Chofu, Tokyo 182-8585, Japan

## HIGHLIGHTS

- Secondary-atom-doped strategy was proposed to synthesize single-atom electrocatalyst.
- The increase in both the density of active sites and their intrinsic activity was achieved simultaneously.
- The resultant single-atom catalyst shows outstanding ORR activity in acidic media.

**ABSTRACT** Single-atom catalysts (SACs) with nitrogen-coordinated nonprecious metal sites have exhibited inimitable advantages in electrocatalysis. However, a large room for improving their activity and durability remains. Herein, we construct atomically dispersed Fe sites in N-doped carbon supports by secondary-atom-doped strategy. Upon the secondary doping, the density and coordination environment of active sites can be efficiently tuned, enabling the simultaneous improvement in the number and reactivity of the active site. Besides, structure optimizations in terms of the enlarged surface area and improved hydrophilicity can be achieved simultaneously. Due to the beneficial microstructure and abundant highly active FeN<sub>5</sub> moieties resulting from the secondary doping, the resultant catalyst exhibits an admirable half-wave potential of 0.81 V versus 0.83 V for Pt/C and much better stability than Pt/C in acidic media. This work would offer a general strategy for the design and preparation of highly active SACs for electrochemical energy devices.



**KEYWORDS** Single-atom catalysts; Fe–N–C catalysts; Doping; Porous nanostructures; Oxygen reduction reaction



## 1 Introduction

Tremendous efforts have been devoted to the exploration of environment-friendly and sustainable energy conversion [1–4]. Among the various options of devices, the sustainable and clean fuel cells involving electrochemical oxygen reduction reaction (ORR) have been regarded as promising energy conversion applications [5–8]. So far, Pt-based catalysts with superior activity are promising electrocatalysts for the ORR [9–12]. However, their prohibitive cost, scarcity and instability call for nonprecious metal catalysts (NPMCs) that have the advantages of natural abundance and low cost [13–17]. In this context, single-atom catalysts (SACs) with nitrogen-coordinated transition metal sites and maximized atom-utilization efficiency, for example, M–N–C (M = Fe, Co, Ni, etc.), are emerging as a promising candidate for the ORR [18–22]. The tailored electronic structure and coordination environments of SACs bring new possibilities for improving ORR performance and fundamental understanding of active centers due to their structural simplicity [23–25]. An annealing process has been demonstrated for the effective formation of active metal centers, which however causes the difficulty in controlling the microstructure/porosity and coordination environment of the SACs [26–28]. Furthermore, to achieve atomic dispersion of metal atoms, SACs usually have a very low density of metal sites that limits catalytic performance in practical devices.

To overcome these limitations of SACs, several strategies have been developed to improve catalytic activity [29–36]. Introducing heteroatoms (N, B, P, and S, etc.) or defect in materials can change the coordination environments of metal sites and thus improve the intrinsic activity of active site, which have been evidenced the effectiveness of enhancing the ORR performance of SACs [30, 37–39]. In addition to optimizing their intrinsic activity of active sites, tuning the number of active sites is also important. Structure design, such as size or morphology control, can improve the exposed area and density of active sites, whereas this strategy is difficult in tuning the coordination environment and intrinsic activity of metal centers [37, 40, 41]. Despite a significant advance in developing SACs, the methods of enhancing concentration and regulating the coordination environment of metal sites simultaneously are still rarely reported. Besides the above, engineering microstructure and hydrophobic/hydrophilic properties of catalysts can significantly realize a high ORR performance [42].

Herein, we reported a secondary-atom-doped strategy to synthesize atomical Fe sites dispersed in carbon support catalysts (Fe–N–C/FeN). Through combining dual-template synthetic strategy involving silica sols as hard templates and  $\text{ZnCl}_2$  as a pore-forming agent, Fe–N–C was first prepared by the pyrolysis and acid leaching. Then, the secondary-atom-doping involving the second thermal activation in the presence of metal salt and nitrogen precursor was carried out to synthesize Fe–N–C/FeN. The final catalyst exhibits an enlarged specific surface area and improved hydrophilicity, which could offer more active sites and make active sites accessible. Significantly, the secondary-atom-doping process enables to simultaneously tune the density and the coordination environment of the single atoms, achieving the goal of substantially boosting catalytic activity. As expected, the as-synthesized Fe–N–C/FeN possesses a remarkable electrocatalytic activity in acidic solution with the remarkable onset potential ( $E_{\text{onset}}$ , 0.85 V) and half-wave potential ( $E_{1/2}$ , 0.81 V) and high stability with scarcely any decay in  $E_{1/2}$  after 30,000 cycles, which exhibit comparable activity but superior stability relative to commercial Pt/C.

## 2 Experimental Section

### 2.1 Physical Characterizations

The morphology of the as-prepared samples was studied by transmission electron microscope (TEM, JEM-2100 HR), high-angle annular dark-field scanning transmission electron microscopy and elemental distribution mappings (HAADF-STEM and EDS mappings, a JEOL 2100F electron microscope). The phase analysis was measured by Raman spectrometer (J-Y T64000), the X-ray diffraction (XRD, X'Pert PRO MRD) and the X-ray photoelectron spectrometer (XPS, PHI-5702). Brunauer–Emmett–Teller (BET) operated on ASAP 2020. The synchrotron-based X-ray absorption spectroscopy (XAS) data were processed by IFEFFIT software.

### 2.2 Materials Preparation

2 g D-glucosamine hydrochloride,  $\text{ZnCl}_2$  and  $\text{FeCl}_3$  with molar ratios (10: 2: 1) were dissolved in 20 mL colloidal silica suspension (2 g  $\text{SiO}_2$ ) with stirring for 10 min. After freeze-dried, the as-prepared samples were heated to 900 °C

for 2 h in the atmosphere of  $N_2$  at  $5\text{ }^\circ\text{C min}^{-1}$  (ramping rate). The as-obtained material was treated with HF (10 wt%) etching for 12 h and the following drying. The black product is labeled as Fe–N–C.

Afterward, 0.4 g Fe–N–C, 26.3 mg  $FeCl_3$  and 0.4 g dicyandiamide were mixed with 20 mL of water and 20 mL of isopropanol by 2 h ultrasound and 5 h stirred, then dried at  $60\text{ }^\circ\text{C}$ . The precursor was annealed at  $900\text{ }^\circ\text{C}$  with  $3\text{ }^\circ\text{C min}^{-1}$  (ramping rate) for 1 h under the atmosphere of  $N_2$ . After the secondary-atom-doping process, the final catalyst was called as Fe–N–C/FeN. For comparison, Fe–N–C/control and Fe–N–C/N catalysts were synthesized through similar procedures with no additional Fe and N source and only additional N source in the second step, respectively.

### 2.3 Electrochemical Experiments

The electrochemical activities were conducted by using a CHI-660 electrochemical analyzer at room temperature. 2 mg of catalysts was dispersed in 5  $\mu\text{L}$  of Nafion (5 wt%), 100  $\mu\text{L}$  of isopropyl alcohol and 400  $\mu\text{L}$  of deionized water by ultrasonic treatment for 30 min to obtain uniform electrocatalyst inks. Then such inks were cast on the surface of rotating disk electrode (RDE) and rotating ring-disk electrode (RRDE) in  $O_2$ -saturated 0.1 M  $HClO_4$  solution with a loading of  $1.0\text{ mg cm}^{-2}$ . The electrochemical active surface area (ECSA) was tested by cyclic voltammetry. Electrochemical impedance spectroscopy (EIS) was measured under AC voltage amplitude of 5 mV and DC voltage based at a given potential at  $10\text{ mA cm}^{-2}$  from 100 kHz to 0.05 Hz. Tafel slopes were calculated as follows:

$$\eta = a + b \log(j/j_0) \quad (1)$$

where  $\eta$ ,  $b$ ,  $j$ , and  $j_0$  are the overpotential, the Tafel slope, the current density, and the exchange current density, respectively. The long-term stability and methanol poisoning experiments were investigated by chronoamperometric measurements. The accelerated durability test (ADT) was investigated by continuous potential cycling between 0.7 and 1 V.

The Koutecky–Levich (K–L) equation was as follows:

$$\frac{1}{J} = \frac{1}{J_L} + \frac{1}{J_K} = \frac{1}{Bw^{1/2}} + \frac{1}{J_K} \quad (2)$$

$$B = 0.2nFC_0D_0^{2/3}V^{-1/6} \quad (3)$$

where  $J$ ,  $J_K$ , and  $J_L$  are the measured current density, kinetic current density and the diffusion-limiting current density, respectively;  $\omega$  is the angular velocity;  $n$  and  $F$  is the electron transfer number and the Faraday constant ( $96485\text{ C mol}^{-1}$ );  $C_0$  and  $D_0$  are the bulk concentration of  $O_2$  ( $1.2 \times 10^{-6}\text{ mol cm}^{-3}$ ) and the diffusion coefficient of  $O_2$  ( $1.9 \times 10^{-5}\text{ cm}^2\text{ s}^{-1}$ );  $V$  is the kinematic viscosity of the electrolyte ( $0.01\text{ cm}^2\text{ s}^{-1}$ ).

The specific kinetic current density can be determined according to the K–L equation:

$$J_K = \frac{J_L * J}{J_L - J} \quad (4)$$

The  $H_2O_2$  yield ( $y$ ) and  $n$  are computed using Eqs. (5) and (6):

$$H_2O_2(\%) = \frac{200I_r/N}{I_r/N + I_d} \quad (5)$$

$$n = \frac{4I_d}{I_r/N + I_d} \quad (6)$$

where  $I_r$  and  $I_d$  are ring and disk current; the current collection efficiency of the Pt ring (N) is 0.37.

The specific value  $S_a$  can be calculated by the related Eqs. (7) and (8):

$$C = I/vm \quad (7)$$

$$S_a = C/C_{GC} \quad (8)$$

where  $v$  is a given scan rate;  $m$  is mass of catalyst deposited on the electrode;  $C$  and  $C_{GC}$  are the gravimetric double-layer capacitance ( $F\text{ g}^{-1}$ ) and the double-layer capacitance ( $F\text{ m}^{-2}$ ) of the electrode surface, respectively.

## 3 Results and Discussion

### 3.1 Materials Characterizations

The Fe–N–C/FeN catalyst was successfully synthesized via a two-step pyrolysis process (Fig. 1a). First, Fe–N–C was synthesized by using a dual-template strategy according to our previous report [43]. Typically, silica sol suspension,  $ZnCl_2$ ,  $FeCl_3$ , and glucosamine were mixed

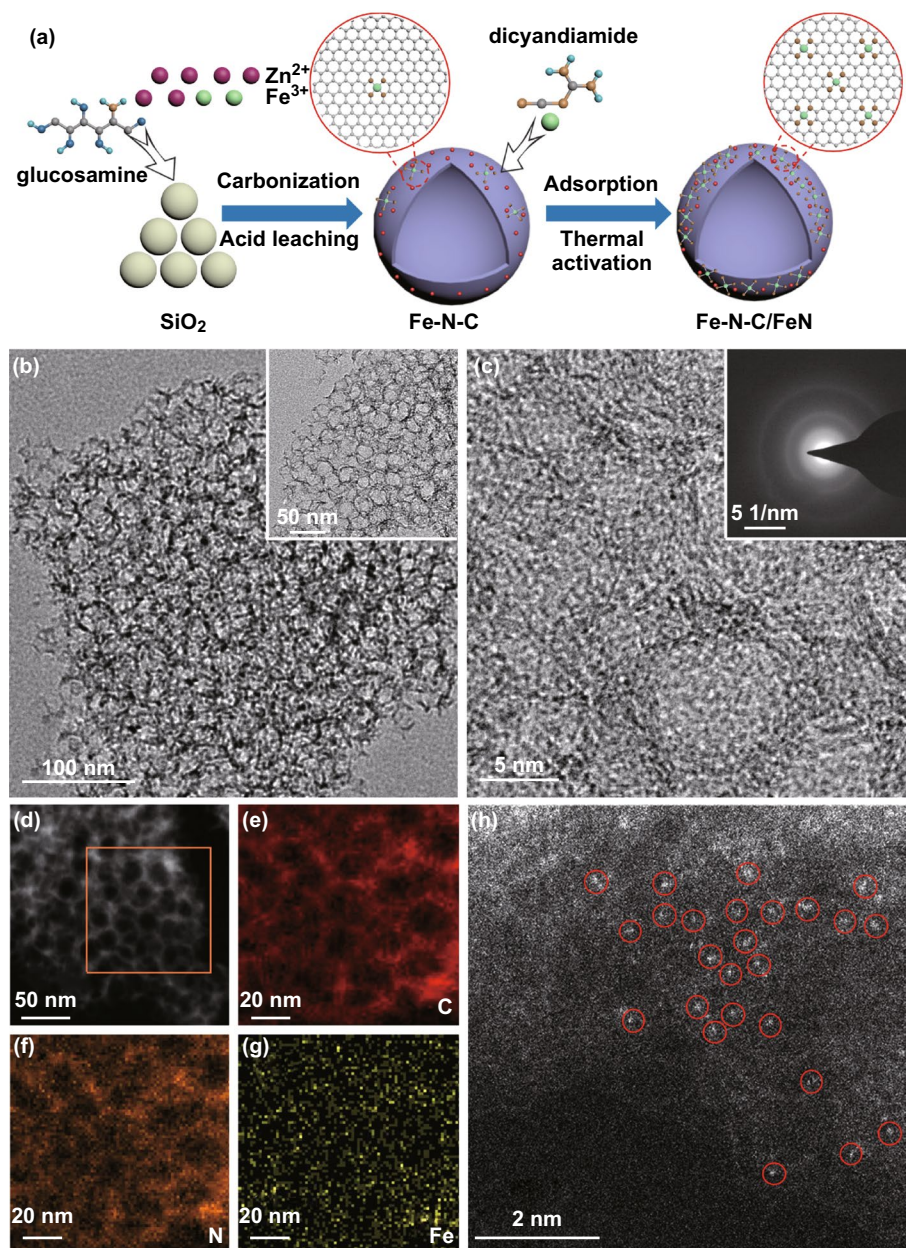


**Fig. 1** **a** Schematic illustration of the synthesis route. **b** TEM and **c** HRTEM images of Fe–N–C/FeN. Inset in **c**: SAED pattern of Fe–N–C/FeN. **d–g** HAADF-STEM and relative elemental mapping images. **h** AC-STEM image of Fe–N–C/FeN

to freezing dry and followed by the pyrolysis and acid leaching. Finally, Fe–N–C/FeN were obtained through the pyrolysis of the mixture of FeCl<sub>3</sub> and dicyandiamide in the presence of the as-prepared Fe–N–C. As revealed in Fig. 1b, TEM image of Fe–N–C/FeN shows that the catalyst was composed of hierarchically spherical pores with the size of about 20 nm, which inherits the morphology of silica nanospheres. HRTEM image in Fig. 1c

shows that the thickness of graphene layers of Fe–N–C/FeN is around 2 nm and no nanoparticles or clusters can be observed. As expected, Fe–N–C/N, Fe–N–C/control, and Fe–N–C show similar morphology to Fe–N–C/FeN, revealing that the secondary-doped atoms did not affect the original morphology (Fig. S1). The ring-like selected area electron diffraction (SAED) pattern verifies the low crystallinity of the sample, demonstrating the disordered

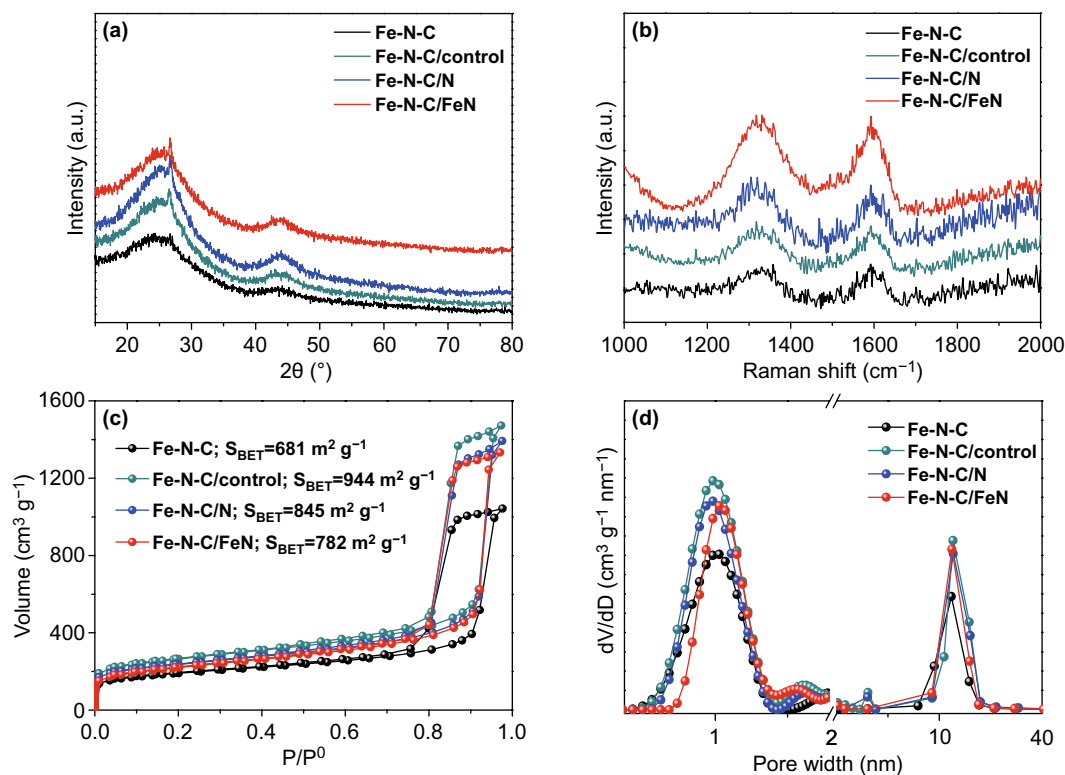


**Fig. 2** **a** XRD patterns, **b** Raman spectra, **c** nitrogen adsorption–desorption isotherm curves and **d** the corresponding pore size distribution curves of the resultant catalysts

stack of graphene layers (inset in Fig. 1c). As revealed in Fig. 1d–g, HAADF-STEM and corresponding EDS mappings were conducted, where Fe, C, and N elements are uniformly dispersed. The aberration-corrected scanning transmission electron microscope (AC-STEM) image reveals that Fe single atoms with brighter spots marked are facily observed over the hierarchically porous structures (Fig. 1h).

As shown in XRD patterns, the catalysts show two distinct peaks at  $25^\circ$  and  $43^\circ$  (Fig. 2a), which are identified as a certain degree of graphitized carbon structures [37]. Except for the two graphitized carbon peaks, no other peaks ascribed to Fe species were observed, indicating the single-atom features of the resultant carbon structures. Fe–N–C/FeN and Fe–N–C/N had a similar crystal structure to Fe–N–C, further suggesting the secondary-doped Fe or N atoms did not destroy the overall structure of supports. Furthermore, the obtained catalysts were characterized by Raman spectra. Two sharp characteristic peaks of these catalysts in accordance with the characteristic D band at  $1350\text{ cm}^{-1}$  and G band at  $1580\text{ cm}^{-1}$  were assigned

to the lattice defects and  $sp^2$ -hybridized carbon, respectively (Fig. 2b). The intensity ratio of D to G band ( $I_D/I_G$ ) manifests the degree of graphitization of carbon materials [44]. Among the as-synthesized catalysts, the  $I_D/I_G$  (1.25) of Fe–N–C/FeN is higher than those of Fe–N–C (0.86), Fe–N–C/control (1.05) and Fe–N–C/N (1.06). This result manifests that the introduction of secondary-doped atoms can be capable of generating more abundant defects, benefiting the exposure of active sites [45]. The  $\text{N}_2$  adsorption–desorption curves of catalysts exhibit a type-IV isotherm, revealing the catalysts possess micropores and mesopores structure (Fig. 2c). It was observed that the BET surface area of the resultant catalysts increased in the following order: Fe–N–C ( $681\text{ m}^2\text{ g}^{-1}$ ) < Fe–N–C/FeN ( $782\text{ m}^2\text{ g}^{-1}$ ) < Fe–N–C/N ( $845\text{ m}^2\text{ g}^{-1}$ ) < Fe–N–C/control ( $944\text{ m}^2\text{ g}^{-1}$ ). BET surface areas of all catalysts subjected to second thermal treatment are larger than that of Fe–N–C, manifesting that the second thermal activation can effectively improve the surface area of materials. Further observation reveals that the secondary-doped N source leads to the decrease in the surface area of materials

relative to Fe–N–C/control, and the surface area further decreases after secondary-doped Fe and N source. Based on the pore size distribution (Fig. 2d), the mesopore distribution of Fe–N–C/FeN is similar to that of Fe–N–C. As for the micropore distribution, Fe–N–C only possesses one micropore located at 1.1 nm, which attributes to the evaporation of Zn at high temperatures [46]. However, Fe–N–C/control, Fe–N–C/N, and Fe–N–C/FeN display an extra micropore located at 1.5 nm, which may attribute to the

second thermal activation. Compared with Fe–N–C/control, Fe–N–C/N and Fe–N–C/FeN exhibited the decrease in micropores and mesopores volume, which may attribute to that Fe and N sources are stabilized in the micropores and mesopores via possible coordination (Table S1) [47]. These results further confirmed that Fe–N–C/FeN possesses the hierarchically porous structure and high surface area, which could offer ample space to improve the density of active sites and promote the transport of proton [46].

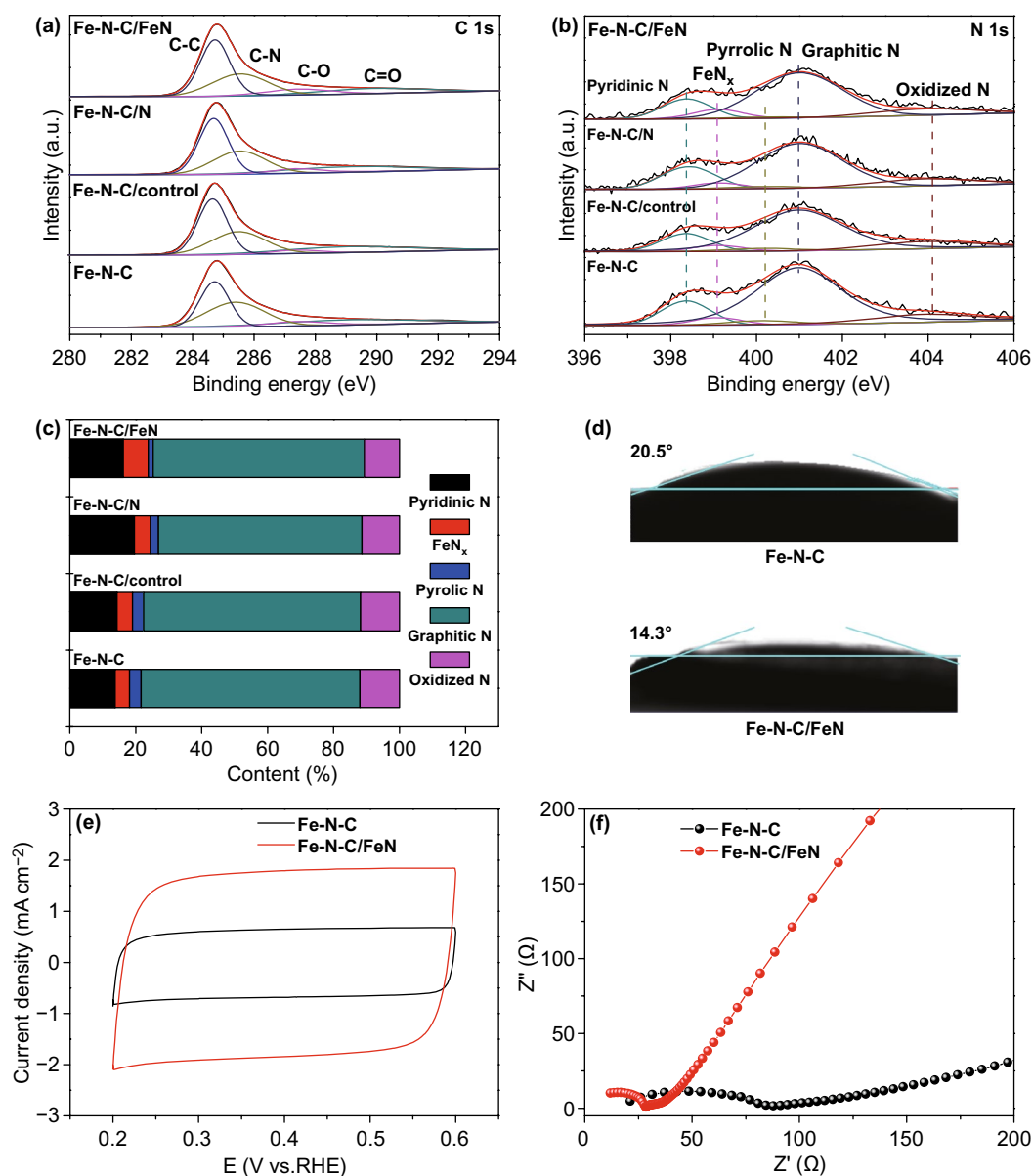


**Fig. 3** a C 1s, b N 1s XPS spectra, and c corresponding contents of different N species of the resultant catalysts. d Water contact angle of Fe–N–C and Fe–N–C/FeN. e Cyclic voltammetry curves in N<sub>2</sub>-saturated HClO<sub>4</sub> solution (sweep rate: 10 mV s<sup>-1</sup>). f EIS curves of Fe–N–C and Fe–N–C/FeN

To analyze the effect of secondary-atom-doping on the compositions and chemical states, XPS was performed. As expected, the C content of Fe–N–C/FeN increases in comparison with Fe–N–C, while the O and N content in the catalysts decreases, which may be attributed to the repairs of carbon supports at the second pyrolysis process. (Table S2) [47]. The high-resolution C 1s spectrum of Fe–N–C/FeN (Fig. 3a) exhibits four different C species, corresponding to C–C (289.8 eV), C–N (287.4 eV), C–O (285.5 eV), and C=O group (284.7 eV), respectively [48, 49]. The C–C species content increases after the second thermal activation, which may be attributed to the increase of C content (Table S3). As for the high-resolution N 1s spectrum of Fe–N–C/FeN (Fig. 3b), it could be deconvoluted with five peaks at 398.3 (pyridinic-N), 399.1 (FeN<sub>x</sub>), 400.1 (pyrrolic-N), 401.0 (graphitic-N), and 403.9 eV (oxidized N), respectively [50]. Although the N content decreased, the percentage of FeN<sub>x</sub> increased from 4.3% (Fe–N–C) to 7.6% (Fe–N–C/FeN) during the second thermal activation in Fig. 3c and Table S4. In addition to forming additional FeN<sub>x</sub>, the secondary-doped N atoms also benefit the transformation of pyrrolic-N into pyridinic-N, which can promote the electrochemical ORR activity in acidic media [51]. Inductively coupled plasma-mass spectrometry (ICP-MS) test was performed to confirm the content of Fe single atoms (Table S5). The Fe content of Fe–N–C/FeN (0.38 wt%) is twice higher than that of Fe–N–C, indicating additional Fe atoms was successfully doped in initial material. Thanks to the advantageous structure and composition, the hydrophilicity has been significantly improved after the second doping by

the contact angle (CA) measurement. As shown in Fig. 3d, the contact angle (14.3°) of Fe–N–C/FeN was smaller than that of Fe–N–C (20.5°), which is proved to facilitate the accessibility of active sites to the electrolyte [42]. ECSA was investigated to further estimate the intrinsic activity of the active sites (Fig. 3e). The ECSA of Fe–N–C/FeN (910 cm<sup>2</sup> g<sup>-1</sup>) is about 3 times larger than that of Fe–N–C, manifesting that the secondary-atom dopant in Fe–N–C/FeN leads to the higher intrinsic activity. Besides, the improved electrical conductivity of Fe–N–C/FeN was characterized by EIS (Fig. 3f). The charge transfer resistance ( $R_{ct}$ ) between electrolyte and catalyst is in connection with the semicircle region of Nyquist plots. Compared with Fe–N–C, Fe–N–C/FeN possesses a small  $R_{ct}$ , indicating that the optimized porous nanostructures caused by secondary-atom-doping are also beneficial to electron transport.

The information on the valence state and coordination environment of Fe centers was examined by XAS. The X-ray absorption near-edge structure (XANES) of Fe K-edge spectra reveals that the Fe-K edge energies of Fe–N–C/control, Fe–N–C/N and Fe–N–C/FeN are all between those of Fe foil (Fe<sup>0</sup>) and Fe<sub>2</sub>O<sub>3</sub> (Fe<sup>3+</sup>) (Fig. 4a), indicating a low oxidation valence of Fe single atoms. The Fourier-transformed (FT)  $k^3$ -weighted extended X-ray absorption fine structure (EXAFS) shows that all Fe–N–C catalysts exhibit only a prominent peak at 1.5 Å (Fig. 4b), attributed to the Fe–N(O) coordination shell. There are no any other bonds, such as Fe–Fe bonds can be observed in the EXAFS, indicating the atomically dispersed feature. The structural parameters from EXAFS fitting reveal the weighted average of Fe–N

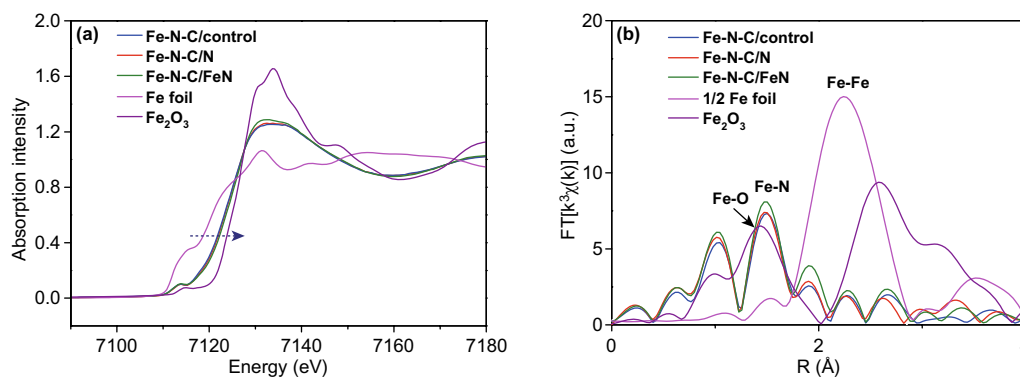


**Fig. 4** **a** K-edge XANES spectra and **b** Fourier-transform EXAFS spectra of Fe–N–C, Fe–N–C/control, Fe–N–C/N, Fe–N–C/FeN, Fe foil, and Fe<sub>2</sub>O<sub>3</sub>

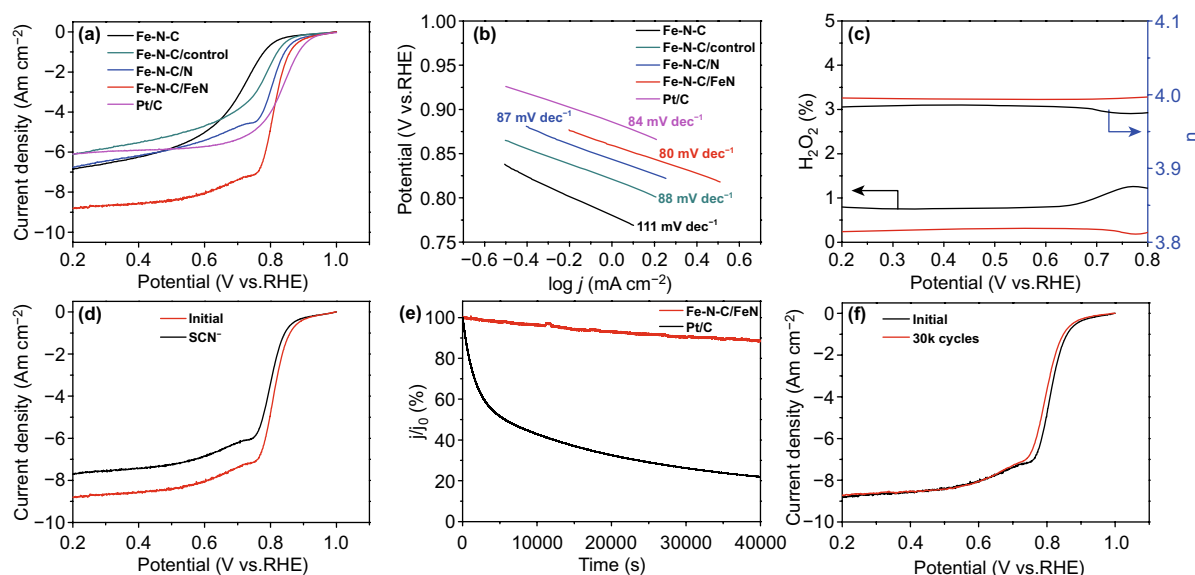


**Fig. 5** **a** LSV curves and **b** Tafel slope curves of Fe-N-C, Fe-N-C/control, Fe-N-C/N, Fe-N-C/FeN and commercial Pt/C at 1600 rpm in O<sub>2</sub>-saturated 0.1 M HClO<sub>4</sub> solution (sweep rate: 10 mV s<sup>-1</sup>). **c** H<sub>2</sub>O<sub>2</sub> yield and electron transfer number of Fe-N-C/FeN (black) and commercial Pt/C (red). **d** LSV curves of Fe-N-C/FeN obtained without and with 5 mM KSCN. **e** Chronoamperometric response of Fe-N-C/FeN and commercial Pt/C. **f** ORR polarization plots of Fe-N-C/FeN before and after 30,000 cycles

coordination number for Fe-N-C/control, Fe-N-C/N, and Fe-N-C/FeN are 4.7, 4.9, and 5.4 (Table S6), respectively. It is suggested that a square-pyramid-like Fe-N<sub>5</sub> configuration with a fifth axial ligand is dominated in the resultant catalysts, which is different from Fe-N-C with a coordination number of about 2.1 [43].

### 3.2 Electrochemical Measurements

The linear sweep voltammetry (LSV) curves reveal that Fe-N-C/FeN possesses an excellent electrocatalytic activity with an  $E_{\text{onset}}$  of 0.96 V and  $E_{1/2}$  of 0.81 V (Fig. 5a), which are superior to those of Fe-N-C/N (0.96 and 0.80 V), Fe-N-C/control (0.93 and 0.78 V), Fe-N-C (0.93 and 0.72 V) and comparable to that of commercial Pt/C (0.96 and 0.83 V) (Table S7). Tafel plots of those catalysts derived from their polarization curves. As revealed in Fig. 5b, Fe-N-C/FeN possesses the smallest Tafel slope (80 mV dec<sup>-1</sup>), manifesting the fast kinetic of Fe-N-C/FeN for ORR process. To corroborate the superior activity of Fe-N-C/FeN, the kinetic current density of Fe-N-C/FeN (11.24 mA cm<sup>-2</sup>) is higher than those of Fe-N-C/N (5.85 mA cm<sup>-2</sup>), Fe-N-C/control (2.40 mA cm<sup>-2</sup>) and Fe-N-C (0.73 mA cm<sup>-2</sup>) via K-L equation (Table S7). As shown in Fig. 5c, electron transfer number ( $n$ ) of Fe-N-C/

FeN is about 4.0 with a low H<sub>2</sub>O<sub>2</sub> yield of below 1% over the entire potential range, which is close to those of commercial Pt/C, revealing a desirable 4e<sup>-</sup> pathway. To further confirm the role of FeN<sub>x</sub>, the SCN<sup>-</sup> poison experiment was also carried out to block the Fe-N sites (Fig. 5d). After the introduction of SCN<sup>-</sup>, the  $E_{1/2}$  of Fe-N-C/FeN is found to shift negatively and diffusion-limiting current density is also decreased, further manifesting that the FeN<sub>x</sub> is the active site for ORR. To investigate the methanol tolerance property and electrochemical stability, the chronoamperometry test was performed. After the addition of 1.0 M methanol, the current line of commercial Pt/C suffers the obvious change (Fig. S2). In contrast, the current of Fe-N-C/FeN remains nearly constant, which indicates that the resultant catalyst possesses strong tolerance to methanol. In the long-term stability test by chronoamperometric, 90% of the initial ORR activity was retained, which is better than that of commercial Pt/C under the same period time (Fig. 5e). Notably, the  $E_{1/2}$  of Fe-N-C/FeN is only observed with a slightly negative shift (19 mV) compared with initial ORR activities of Fe-N-C/FeN after 30,000 cycles (Fig. 5f), indicating the best ORR stability. Compared with the other reported NPMCs in acidic media, Fe-N-C/FeN displays the excellent electrochemical activity (Table S8).



Recent density functional theory (DFT) calculations showed FeN<sub>5</sub> moiety in acidic media has a lower reaction energy barrier than other low coordinated FeN<sub>x</sub> moieties [50, 52]. The lower energy barrier indicates good ORR activities because it makes O<sub>2</sub> easier to be reduced to H<sub>2</sub>O. In addition, the adsorption energy of OH also has a contribution to improve the electrocatalytic activity [53, 54]. According to the previous reports, DFT calculations indicated that FeN<sub>5</sub> sites have a lower reaction energy barrier (0.67 eV) and adsorption energy of intermediate OH (2.88 eV) compared with FeN<sub>4</sub> sites (0.75 and 3.07 eV) or FeN<sub>2</sub> sites (1.99 and 4.38 eV), facilitating the ORR activity in acid media [50]. It is believed that FeN<sub>5</sub> sites have more effective ORR activity than FeN<sub>4</sub> and FeN<sub>2</sub> sites via DFT calculation. Experimental results and DFT calculations manifest that the outstanding ORR performance of the catalyst is significantly correlated with tuning the density and coordination environment of active sites.

## 4 Conclusions

In summary, a secondary-atom-doped strategy was manipulated to fabricate atomical Fe sites dispersed in carbon support catalysts. Besides the optimization of microstructures and hydrophobic/hydrophilic properties of catalysts, the density and coordination environment of Fe sites in Fe–N–C/FeN catalyst also were optimized simultaneously during the secondary doping process. The obtained Fe–N–C/FeN showed comparable activity and high long-term stability for ORR relative to Pt/C in acidic electrolytes. Experimental results further confirmed that FeN<sub>5</sub> sites have more effective ORR activity than FeN<sub>2</sub> sites, in agreement with the DFT calculations. This work opens a new insight into rational design of robust SACs with enhanced intrinsic activity and high density of active sites, holding great promise in energy-related small-molecule electrocatalysis.

**Acknowledgements** The authors gratefully acknowledge the financial support of the Fundamental Research Funds for the Central Universities (CCNU20QN007, CCNU20TS013), the Program of Introducing Talents of Discipline to Universities of China (111 program, B17019) and the Recruitment Program of Global Youth Experts of China.

**Open Access** This article is licensed under a Creative Commons Attribution 4.0 International License, which permits use, sharing, adaptation, distribution and reproduction in any medium or format,

as long as you give appropriate credit to the original author(s) and the source, provide a link to the Creative Commons licence, and indicate if changes were made. The images or other third party material in this article are included in the article's Creative Commons licence, unless indicated otherwise in a credit line to the material. If material is not included in the article's Creative Commons licence and your intended use is not permitted by statutory regulation or exceeds the permitted use, you will need to obtain permission directly from the copyright holder. To view a copy of this licence, visit <http://creativecommons.org/licenses/by/4.0/>.

**Electronic supplementary material** The online version of this article (<https://doi.org/10.1007/s40820-020-00502-5>) contains supplementary material, which is available to authorized users.

## References

1. J. Li, S. Sharma, X. Liu, Y.-T. Pan, J.S. Spendlow et al., Hard-magnet L10-CoPt nanoparticles advance fuel cell catalysis. *Joule* **3**(1), 124–135 (2019). <https://doi.org/10.1016/j.joule.2018.09.016>
2. J. Liu, D. Zhu, Y. Zheng, A. Vasileff, S.-Z. Qiao, Self-supported earth-abundant nanoarrays as efficient and robust electrocatalysts for energy-related reactions. *ACS Catal.* **8**(7), 6707–6732 (2018). <https://doi.org/10.1021/acscatal.8b01715>
3. W.-J. Liu, H. Jiang, H.-Q. Yu, Emerging applications of biochar-based materials for energy storage and conversion. *Energy Environ. Sci.* **12**(6), 1751–1779 (2019). <https://doi.org/10.1039/C9EE00206E>
4. S.K. Singh, K. Takeyasu, J. Nakamura, Active sites and mechanism of oxygen reduction reaction electrocatalysis on nitrogen-doped carbon materials. *Adv. Mater.* **31**, 1804297 (2019). <https://doi.org/10.1002/adma.201804297>
5. X. Luo, X. Wei, H. Zhong, H. Wang, Y. Wu et al., Single-atom Ir-anchored 3D amorphous NiFe nanowire@nanosheets for boosted oxygen evolution reaction. *ACS Appl. Mater. Interfaces* **12**(3), 3539–3546 (2020). <https://doi.org/10.1021/acsmi.9b17476>
6. Y. Guo, T. Park, J. Yi, J. Henzie, J. Kim et al., Nanoarchitectonics for transition-metal-sulfide-based electrocatalysts for water splitting. *Adv. Mater.* **31**(17), 1807134 (2019). <https://doi.org/10.1002/adma.201807134>
7. Y. Guo, J. Tang, H. Qian, Z. Wang, Y. Yamauchi, One-pot synthesis of zeolitic imidazolate framework 67-derived hollow Co<sub>3</sub>S<sub>4</sub>@MoS<sub>2</sub> heterostructures as efficient bifunctional catalysts. *Chem. Mater.* **29**(13), 5566–5573 (2017). <https://doi.org/10.1021/acs.chemmater.7b00867>
8. Y. Guo, J. Tang, Z. Wang, Y. Kang, Y. Bando, Y. Yamauchi, Elaborately assembled core-shell structured metal sulfides as a bifunctional catalyst for highly efficient electrochemical overall water splitting. *Nano Energy* **47**, 494–502 (2018). <https://doi.org/10.1016/j.nanoen.2018.03.012>



9. X. Luo, X. Wei, H. Wang, Y. Wu, W. Gu, C. Zhu, Hexamine-coordination-framework-derived Co-N-doped carbon nanosheets for robust oxygen reduction reaction. *ACS Sustain. Chem. Eng.* **8**(26), 9721–9730 (2020). <https://doi.org/10.1021/acssuschemeng.0c01826>
10. C. Xuan, J. Wang, J. Zhu, D. Wang, Recent progress of metal organic frameworks-based nanomaterials for electrocatalysis. *Acta Phys. Chim. Sin.* **33**(1), 149–164 (2017). <https://doi.org/10.3866/PKU.WHXB201609143>
11. X. Wei, X. Luo, H. Wang, W. Gu, W. Cai, Y. Lin, C. Zhu, Highly-defective Fe-N-C catalysts towards pH-universal oxygen reduction reaction. *Appl. Catal. B: Environ.* **263**, 118347 (2019). <https://doi.org/10.1016/j.apcatb.2019.118347>
12. C. Chen, X. Zhang, Z. Zhou, X. Zhang, S. Sun, Experimental boosting of the oxygen reduction activity of an Fe/N/C Catalyst by sulfur doping and density functional theory calculations. *Acta Phys. Chim. Sin.* **33**(9), 1875–1883 (2017). <https://doi.org/10.3866/PKU.WHXB201705088>
13. S. Ahn, X. Yu, A. Manthiram, “Wiring” Fe-N<sub>x</sub>-embedded porous carbon framework onto 1D nanotubes for efficient oxygen reduction reaction in alkaline and acidic media. *Adv. Mater.* **29**, 1606534 (2017). <https://doi.org/10.1002/adma.201606534>
14. J. Guo, C.-Y. Lin, Z. Xia, Z. Xiang, A pyrolysis-free covalent organic polymer for oxygen reduction, a pyrolysis-free covalent organic polymer for oxygen reduction. *Angew. Chem. Int. Ed.* **130**, 12747–12752 (2018). <https://doi.org/10.1002/anie.201808226>
15. J.-I. Jung, M. Risch, S. Park, M.G. Kim, G. Nam et al., Optimizing nanoparticle perovskite for bifunctional oxygen electrocatalysis. *Energy Environ. Sci.* **9**, 176–183 (2016). <https://doi.org/10.1039/C5EE03124A>
16. W. Xia, R. Zou, L. An, D. Xia, S. Guo, A metal-organic framework route to in situ encapsulation of Co@Co<sub>3</sub>O<sub>4</sub>@C core@bireshell nanoparticles into a highly ordered porous carbon matrix for oxygen reduction. *Energy Environ. Sci.* **8**, 568–576 (2015). <https://doi.org/10.1039/C4EE02281E>
17. J. Zhang, Z. Zhao, Z. Xia, L. Dai, A metal-free bifunctional electrocatalyst for oxygen reduction and oxygen evolution reactions. *Nat. Nanotechnol.* **10**(5), 444–452 (2015). <https://doi.org/10.1038/nnano.2015.48>
18. H. Hu, L. Han, M. Yu, Z. Wang, X. Lou, Metal-organic-framework-engaged formation of Co nanoparticle-embedded carbon@Co<sub>9</sub>S<sub>8</sub> double-shelled nanocages for efficient oxygen reduction. *Energy Environ. Sci.* **9**, 107–111 (2016). <https://doi.org/10.1039/C5EE02903A>
19. Y. Wang, Y.J. Tang, K. Zhou, Self-adjusting activity induced by intrinsic reaction intermediate in Fe-N-C single-atom catalysts. *J. Am. Chem. Soc.* **141**(36), 14115–14119 (2019). <https://doi.org/10.1021/jacs.9b07712>
20. X. Sun, S. Sun, S. Gu, Z. Liang, J. Zhang et al., High-performance single atom bifunctional oxygen catalysts derived from ZIF-67 superstructures. *Nano Energy* **61**, 245–250 (2019). <https://doi.org/10.1016/j.nanoen.2019.04.076>
21. X. Wang, Z. Li, Y. Qu, T. Yuan, W. Wang, Y. Wu, Y. Li, Review of metal catalysts for oxygen reduction reaction: from nanoscale engineering to atomic design. *Chem* **5**(6), 1486–1511 (2019). <https://doi.org/10.1016/j.chempr.2019.03.002>
22. L. Hu, X. Zeng, X. Wei, H. Wang, W. Yu et al., Interface engineering for enhancing electrocatalytic oxygen evolution of NiFe LDH/NiTe heterostructures. *Appl. Catal. B: Environ.* **273**(15), 119014 (2020). <https://doi.org/10.1016/j.apcatb.2020.119014>
23. Y. Qian, Q. Liu, E. Sarnello, C. Tang, M. Chng et al., MOF-derived carbon networks with atomically dispersed Fe-N<sub>x</sub> sites for oxygen reduction reaction catalysis in acidic media. *ACS Mater. Lett.* **1**(1), 37–43 (2019). <https://doi.org/10.1021/acsmaterialslett.9b00052>
24. Z. Chen, W. Gong, Z. Liu, S. Cong, Z. Zheng et al., Coordination-controlled single-atom tungsten as a non-3d-metal oxygen reduction reaction electrocatalyst with ultrahigh mass activity. *Nano Energy* **60**, 394–403 (2019). <https://doi.org/10.1016/j.nanoen.2019.03.045>
25. Z. Li, H. He, H. Cao, S. Sun, W. Diao et al., Atomic Co/Ni dual sites and Co/Ni alloy nanoparticles in N-doped porous Janus-like carbon frameworks for bifunctional oxygen electrocatalysis. *Appl. Catal. B: Environ.* **240**, 112–121 (2019). <https://doi.org/10.1016/j.apcatb.2018.08.074>
26. J. Li, S. Chen, W. Li, R. Wu, S. Ibraheem et al., A eutectic salt-assisted semi-closed pyrolysis route to fabricate high-density active-site hierarchically porous Fe/N/C catalysts for the oxygen reduction reaction. *J. Mater. Chem. A* **6**, 15504–15509 (2018). <https://doi.org/10.1039/C8TA05419C>
27. J. Li, S. Chen, N. Yang, M. Deng, S. Ibraheem et al., Ultrahigh-loading zinc single-atom catalyst for highly efficient oxygen reduction in both acidic and alkaline media. *Angew. Chem. Int. Ed.* **58**(21), 7035–7039 (2019). <https://doi.org/10.1002/anie.201902109>
28. H. Jiang, Y. Liu, W. Li, J. Li, Co Nanoparticles confined in 3D nitrogen-doped porous carbon foams as bifunctional electrocatalysts for long-life rechargeable zn-air batteries. *Small* **14**(13), 1703739 (2018). <https://doi.org/10.1002/sml.201703739>
29. W. Jiao, C. Chen, W. You, J. Zhang, J. Liu, R. Che, Yolk-shell Fe/Fe<sub>4</sub>N@Pd/C magnetic nanocomposite as an efficient recyclable ORR electrocatalyst and SERS substrate. *Small* **15**(7), 1805032 (2019). <https://doi.org/10.1002/sml.201805032>
30. P. Chen, T. Zhou, L. Xing, K. Xu, Y. Tong et al., Atomically dispersed iron-nitrogen species as electrocatalysts for bifunctional oxygen evolution and reduction reactions. *Angew. Chem. Int. Ed.* **56**(2), 610–614 (2017). <https://doi.org/10.1002/anie.201610119>
31. K. Yuan, S. Sfaelou, M. Qiu, D. Lützenkirchen-Hecht, X. Zhuang et al., Pyridinic-N-dominated doped defective graphene as a superior oxygen electrocatalyst for ultrahigh-energy-density Zn-air batteries. *ACS Energy Lett.* **3**(5), 252–260 (2018). <https://doi.org/10.1021/acseenergylett.8b00303>
32. C. Zhu, S. Fu, Q. Shi, D. Du, Y. Lin, Single-atom electrocatalysts. *Angew. Chem. Int. Ed.* **56**(45), 13944–13960 (2017). <https://doi.org/10.1002/anie.201703864>
33. Y. Guo, J. Tang, J. Henzie, B. Jiang, H. Qian et al., Assembly of hollow mesoporous nanoarchitectures composed of ultrafine

- Mo<sub>2</sub>C nanoparticles on N-doped carbon nanosheets for efficient electrocatalytic reduction of oxygen. *Mater. Horiz.* **4**, 1171–1177 (2017). <https://doi.org/10.1039/C7MH00586E>
34. H. Tan, J. Tang, J. Henzie, Y. Li, X. Xu et al., Assembly of hollow carbon nanospheres on graphene nanosheets and creation of iron-nitrogen-doped porous carbon for oxygen reduction. *ACS Nano* **12**, 5674–5683 (2018). <https://doi.org/10.1021/acsnano.8b01502>
35. H. Tan, Y. Li, J. Kim, T. Takei, Z. Wang et al., Sub-50 nm iron-nitrogen-doped hollow carbon sphere-encapsulated iron carbide nanoparticles as efficient oxygen reduction catalysts. *Adv. Sci.* **5**(7), 1800120 (2018). <https://doi.org/10.1002/adv.201800120>
36. W. Xia, J. Tang, J. Li, S. Zhang, K. Wu, J. He, Y. Yamauchi, Defect-rich graphene nanomesh produced by thermal exfoliation of metal-organic frameworks for the oxygen reduction reaction. *Angew. Chem. Int. Ed.* **58**(38), 13354–13359 (2019). <https://doi.org/10.1002/anie.201906870>
37. R. Jiang, L. Li, T. Sheng, G. Hu, Y. Chen, L. Wang, Edge-site engineering of atomically dispersed Fe-N<sub>4</sub> by selective C–N bond cleavage for enhanced oxygen reduction reaction activities. *J. Am. Chem. Soc.* **140**(37), 11594–11598 (2018). <https://doi.org/10.1021/jacs.8b07294>
38. Y. Pan, S. Liu, K. Sun, X. Chen, B. Wang et al., A bimetallic Zn/Fe polyphthalocyanine-derived single-atom Fe-N<sub>4</sub> catalytic site: a superior trifunctional catalyst for overall water splitting and zn-air batteries. *Angew. Chem. Int. Ed.* **57**(28), 8614–8618 (2018). <https://doi.org/10.1002/anie.201804349>
39. Q. Li, W. Chen, H. Xiao, Y. Gong, Z. Li et al., Fe isolated single atoms on S, N codoped carbon by copolymer pyrolysis strategy for highly efficient oxygen reduction reaction. *Adv. Mater.* **30**(25), 1800588 (2018). <https://doi.org/10.1002/adma.201800588>
40. E. Luo, H. Zhang, X. Wang, L. Gao, L. Gong et al., Single-atom Cr-N<sub>4</sub> sites designed for durable oxygen reduction catalysis in acid media. *Angew. Chem. Int. Ed.* **58**(36), 12469–12475 (2019). <https://doi.org/10.1002/anie.201906289>
41. D. Zhao, J.-L. Shui, C. Chen, X. Chen, B.M. Repragle, D. Wang, D.-J. Liu, Iron imidazolate framework as precursor for electrocatalysts in polymer electrolyte membrane fuel cells. *Chem. Sci.* **3**, 3200–3205 (2012). <https://doi.org/10.1039/C2SC20657A>
42. Y. Zhao, X. Li, X. Jia, S. Gao, Why and how to tailor the vertical coordinate of pore size distribution to construct ORR-active carbon materials? *Nano Energy* **58**, 384–391 (2019). <https://doi.org/10.1016/j.nanoen.2019.01.057>
43. C. Zhu, Q. Shi, B.Z. Xu, S. Fu, G. Wan et al., Hierarchically porous M-N-C (M = Co and Fe) single-atom electrocatalysts with robust MN<sub>x</sub> active moieties enable enhanced ORR performance. *Adv. Energy Mater.* **8**(29), 1801956 (2018). <https://doi.org/10.1002/aenm.201801956>
44. X. Liu, J. Kang, Y. Dai, C. Dong, X. Guo, X. Jia, Graphene-like nitrogen-doped carbon nanosheet prepared from direct calcination of dopamine confined by g-C<sub>3</sub>N<sub>4</sub> for oxygen reduction. *Adv. Mater. Interfaces* **5**(14), 1800303 (2018). <https://doi.org/10.1002/admi.201800303>
45. B.-Q. Li, C.-X. Zhao, S. Chen, J.-N. Liu, X. Chen, L. Song, Q. Zhang, Framework-porphyrin-derived single-atom bifunctional oxygen electrocatalysts and their applications in Zn-air batteries. *Adv. Mater.* **31**(19), 1900592 (2019). <https://doi.org/10.1002/adma.201900592>
46. H.-W. Liang, X. Zhuang, S. Brüller, X. Feng, K. Müllen, Hierarchically porous carbons with optimized nitrogen doping as highly active electrocatalysts for oxygen reduction. *Nat. Commun.* **5**, 4973 (2014). <https://doi.org/10.1038/ncomms5973>
47. J. Li, M. Chen, D.A. Cullen, S. Hwang, M. Wang et al., Atomically dispersed manganese catalysts for oxygen reduction in proton-exchange membrane fuel cells. *Nat. Catal.* **1**, 935–945 (2018). <https://doi.org/10.1038/s41929-018-0164-8>
48. H. Jiang, J. Gu, X. Zheng, M. Liu, X. Qiu et al., Defect-rich and ultrathin N doped carbon nanosheets as advanced trifunctional metal-free electrocatalysts for the ORR, OER and HER. *Energy Environ. Sci.* **12**, 322–333 (2019). <https://doi.org/10.1039/C8EE03276A>
49. J. Wang, G. Yin, Y. Shao, Z. Wang, Y. Gao, Investigation of further improvement of platinum catalyst durability with highly graphitized carbon nanotubes support. *J. Phys. Chem. C* **112**(15), 5784–5789 (2008). <https://doi.org/10.1021/jp800186p>
50. Q. Lai, L. Zheng, Y. Liang, J. He, J. Zhao, J. Chen, Metal-organic-framework-derived Fe-N/C electrocatalyst with five-coordinated Fe-N<sub>x</sub> sites for advanced oxygen reduction in acid media. *ACS Catal.* **7**(3), 1655–1663 (2017). <https://doi.org/10.1021/acscatal.6b02966>
51. X. Ao, W. Zhang, Z. Li, J.-G. Li, L. Soule et al., Markedly enhanced oxygen reduction activity of single-atom Fe catalysts via integration with Fe nanoclusters. *ACS Nano* **13**, 11853–11862 (2019). <https://doi.org/10.1021/acsnano.9b05913>
52. Y. Zheng, D.-S. Yang, J.M. Kweun, C. Li, K. Tan et al., Rational design of common transition metal-nitrogen-carbon catalysts for oxygen reduction reaction in fuel cells. *Nano Energy* **30**, 443–449 (2016). <https://doi.org/10.1016/j.nanoen.2016.10.037>
53. Y. Chen, S. Ji, S. Zhao, W. Chen, J. Dong et al., Enhanced oxygen reduction with single-atomic-site iron catalysts for a zinc-air battery and hydrogen-air fuel cell. *Nat. Commun.* **9**(1), 5422 (2018). <https://doi.org/10.1038/s41467-018-07850-2>
54. Q. Jia, N. Ramaswamy, H. Hafiz, U. Tylus, K. Strickland et al., Experimental observation of redox-induced Fe-N switching behavior as a determinant role for oxygen reduction activity. *ACS Nano* **9**(12), 12496–12505 (2015). <https://doi.org/10.1021/acsnano.5b05984>

